The Effect of Wire Feed Speed on the Structure in Electroslag Welding of Low Carbon Steel

Increasing wire or electrode feed rate at constant voltage has no significant effect on penetration but increases pool depth and decreases the shape factor, while increasing welding voltage at constant electrode feed rate increases both pool depth and penetration but has little effect on the shape factor

BY M. SOLARI AND H. BILONI

ABSTRACT. In Electroslag welding of low carbon steel, the effects of electrode feed rate on weld geometry, welding velocity, energy input, weld macrostructure and the microstructure of the weld and HAZ were determined. Results showed that increasing the electrode feed rate at constant voltage had no significant effect on the penetration but increased the pool depth, decreased the shape factor and increased the encounter angle. The pool shape was approximately a paraboloid of revolution. Increasing the welding voltage at constant feed rate increased both pool depth and penetration, but had little effect on the shape factor.

Standard and special metallographic etchants were used to study the transition region between the weld and the base metal, the average dendritic cell diameter, the pool shape and the mechanism of metal transfer from the base metal to the liquid pool as a function of the penetration; results were related to the welding parameters.

Introduction

During the past few years, numerous papers describing the details of electroslag welding (ESW) have been published.[1-5] Essentially, ESW is an automatic arcless welding process, best suited for the joining of plate 2 in. (5 cm) or thicker. Joule heating of an electrically conductive pool of molten slag serves to melt the filler metal together with a portion of the base metal on either side of the joint. The resulting weld pool and the overlying pool of molten slag are contained within the joint by water-cooled copper shoes.

The geometry of the system is such that the solid-liquid interface beneath the weld pool soon assumes a dynamically stable shape which is determined by a combination of welding variables, joint separation, and plate thickness. Once dynamic equilibrium is achieved, the solidification rate and the temperature gradient at the solid-liquid interface depend upon the location on the interface but are independent of time, providing the welding conditions are not changed.

The microstructure of solidified weld metal is known to have a strong influence on the mechanical, physical and chemical properties of the weld.[6-8] The shape of the molten weld pool and the rate of growth at the solid-liquid interface affect both the size and shape of the grains, their relative crystallographic orientation, and both macro- and microsegregation. In electroslag welding, it is possible to define an "encounter angle" which depends upon the shape and depth of the weld pool and affects the sensitivity to centerline hot cracking.[1]

Although it is not possible to observe the shape of the pool during welding, several theoretical and experimental methods have been developed to overcome this difficulty. Essentially, the experimental methods are intended to reveal the position of the S-L interface using different tracers, such as radioactive materials and sulfur additions subsequently revealed by sulfur prints.[9] These methods reveal the shape of the pool at certain moments of the process. On the other hand, theoretical methods have been used by several authors in order to obtain expressions for predicting the pool shape; these are used not only in welding but also in other processes, such as the electroslag remelting process (ESR), which has similar thermal characteristics.[9-11] The mathematical problem is complex enough to require the introduction of several simplifications in order to obtain formal expressions able to describe the pool. A subsequent work will describe a simplified model of the thermal field existing during the electroslag welding operation.

Savage and co-workers have done

M. SOLARI is with the Department of Materials and H. BILONI is Head of the Solidification and Casting Division, Comision Nacional de Energia Atomica, Buenos Aires, Argentina.

extensive studies[8,12,13] on the correlation between welding structures and substructures and the operational variables of different welding processes. The aim of their type of approach is to provide correlations between solidification and phase transformation structures and substructures and the mechanical properties of the weld.

The work described in this paper corresponds to the initiation of studies on the ESW process at the Solidification and Casting Division of the Atomic Energy Commission of Argentina. Its principal goal is to determine the effect of electrode feed rate on the geometry of the weld pool, the welding speed, the energy input and the resultant macro- and microstructure of the weld and HAZ. Different techniques were used in order to reveal the pool shape. In addition, the mechanisms involved in the material transfer from the base metal to the weld region were to be studied.

Carbon steel was used in the experiments in order to develop an improved understanding of both the solidification substructures and the microstructure present in the HAZ region. The results obtained during this research were correlated with the experience accumulated in the laboratory as a result of extensive studies on controlled solidification performed in the past.[14,15]

Experimental Procedure

Equipment

A commercial constant potential dc welding power supply with nominal outputs of 85, 58 and 35 V was used in the reverse polarity mode. The maximum current was varied between 1000 and 1200 A. The equipment enables the use of either one or two electrodes according to the plate thickness; the electrodes can be used with or without oscillation.

Table 1—Chemical Compositions of Base Metal, Electrode, Consumable Guide and Typical Weld Deposit, Wt-%[a]

	C	Mn	Si	S	P
Base metal	.07	.48	.05	.039	.012
Consumable guide	.19	.65	.12	.018	.011
Electrode	.09	1.15	.54	.016	.020
Weld deposit	.11	.79	.24	.030	.016

[a] Balance is Fe.

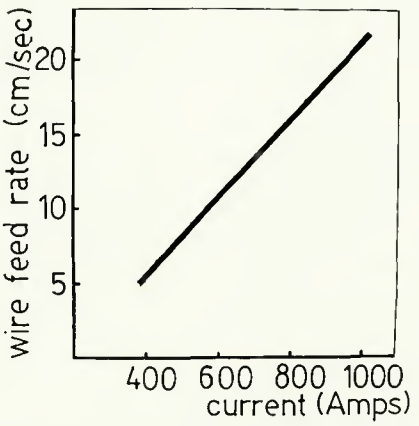

Fig. 1—Relationship between V_e and I for electrode of 0.238 cm diameter.

Material

The chemical composition of the plate, electrode feed and consumable guide used are given in Table 1. The flux used had the following composition: SiO_2—36.29%; MnO_2—27.37%; CaO—16.82%; Al_2O_3—8.72%; MgO—2.67%; TiO_2—2.53%; Fe_2O_3—1.27%; Na_2O—0.93%; K_2O—0.72%.

Welding Procedure

Complete details of welding conditions have been given in previous papers.[16,17] They can be summarized as follows:

1. Constants: Plate size was 35 × 35 × 5.1 cm (13.8 × 13.8 × 2 in.) and the separation between plates to be welded was 2.5 cm (1 in.) at the bottom and 3.0 cm (1.18 in.) at the top, regardless of the plate height. A nominal value of 2.8 cm (1.1 in.) was used in welding velocity calculations. A 0.238 cm (3/32 in.) diameter commercial electrode and one consumable guide were used without oscillation. Slag depth was maintained constant by addition of flux during the operation. A constant voltage of 40 V was used.

2. Welding Speeds and Resulting Weld Currents: The independent variable studied was electrode feed rate V_e over the range from 5 to 19 cm/sec (approx. 2-7.5 ips). This variable controls welding current. Figure 1 shows the relationship between electrode (i.e., wire) feed rate V_e, and weld current, I.

Several factors, such as minor variations in the slag level, periodic fluctuation of the electrode feed rate and stray arcs, caused fluctuations of ± 50 A in the measured weld current.

Measurement of Weld Geometry

Figure 2 shows schematically the metallographic planes upon which the structural analyses were made. The surfaces were prepared by standard mechanical polishing techniques. In order to measure the geometry of the welds, both metallographic and sulfur addition techniques were used.

Metallography. The composition of the etchant was $CuCl_2$—45 g; $FeCl_3$—8 g; HCl—180 cc; HNO_3—1.5 cc; H_2O—180 cc; alcohol—380 cc. The etching was performed at room temperature. A subsequent light repolishing with alumina reveals the segregation and thus delineates the pool shape permitting the measurement of the depth of the pool H, the weld width b, and the "encounter angle" as shown schematically in Fig. 3. The same etching procedure was also used in order to reveal the segregation substructure.

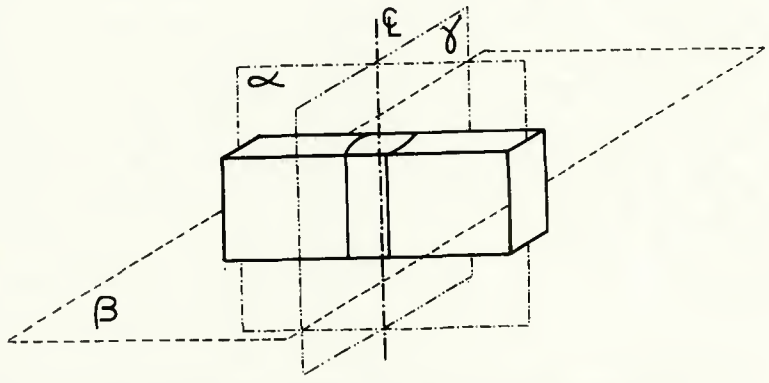

Fig. 2—Schematic representation of the sections metallographically analyzed: α = vertical plane through the midsection of the plate; β = vertical plane through the midsection of the weld and perpendicular to plate surfaces; γ = horizontal cross section of the weld

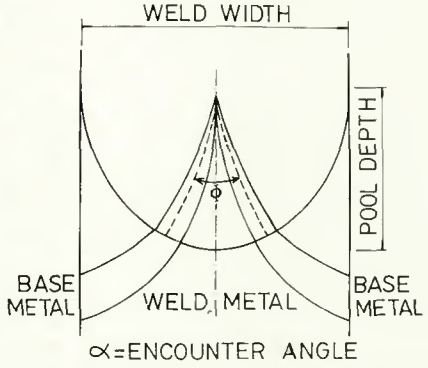

Fig. 3—Schematic representation of a section on plane α; the pool depth H, the weld width b_w and the "encounter angle" are defined

Sulfur Print Technique. In order to make periodic sulfur additions during welding, the insulating rings of the consumable guide were replaced by metallic rings containing 2 g of FeS. When the molten slag reached the rings, the S was incorporated in the weld pool. After welding a sulfur print could then be prepared to reveal the pool profile.

A shape factor* ($\delta = b_w/H$) was calculated; this is considered to be an important parameter influencing the susceptibility to crack formation.[1]

Calculation of Energy Input

The travel speed, V_w, was calculated as follows:

$$V_w = (A_c/A_g) \times V_e$$

A_c is the cross sectional area of the electrode; A_g is the cross sectional area of the gap between the plates to be welded and V_e is the electrode feed rate.

The error involved was estimated as 4%. The most important source of error was the difference between the actual value of A_g and the calculated value with the nominal plate separation, b_g.

The energy input was then calculated as follows:

$$\text{E.I.} = \frac{\text{Volts} \times \text{Current} \times 60}{\text{travel speed (in ipm)} \times 1000} = \text{kJoules/in.}$$

$$\text{and: kJ/cm} = (\text{kJ/in.}) \times 0.394$$

Metallographic Procedures

Macrographic Examination. Both 10% nital and the previously mentioned etchant were used. Either etchant allows the measurement of the encounter angle on the α plane (refer to Fig. 2). The dilution of the weld metal with base metal was measured on the β plane and calculated by means of the expression:

$$D = ((A_w - A_g)/A_w) \times 100$$

where A_w is the cross sectional area of the weld and A_g is the cross sectional area of the original gap between the plates to be welded.

Metallographic Examination. In order to reveal the microstructure and the solidification substructure, two etchants were used: nital 1% and a reagent with the following composition: Cu_2Cl_2—45 g; $FeCl_2$—8 g; HCl—180 cc; HNO_3—2 cc; H_2O—180 cc; alcohol—380 cc. Etching was performed at room temperature.

Both etchants, together with the etchant used to detect the shape of the weld pool, were used in order to study the transition zone between the weld metal and the HAZ, as well as the mechanism involved in the metal transfer from the base metal to the weld pool.

Symbolized here by Greek delta (δ) instead of normally used Greek psi.

Results and Discussion

Table 3 summarizes the experiments performed and the welding conditions, as well as the calculated and measured dependent variables.

Table 2—Welding Procedures

Plate thickness	5.1 cm (2 in.)
Plate separation	2.8 cm (nominal) (1.10 in.)
Electrode diameter	.238 cm (3/32 in.)
Oscillation	none
Number of electrodes	One
Depth of slag pool	4.0 cm (1.57 in.)
Voltage	40 V (open circuit)
Current	450-900 A
Electrode feed rate	5-19 cm/sec (118.11-448.82 ipm)

Effect of Electrode Feed Rate on the Shape of the Pool

Penetration. Table 3 shows that when the welding voltage was held constant the weld width was not greatly influenced by current changes within the range of electrode feed speed studied. Complementary experiments made with 35 and 55 V showed that the welding voltage is the major factor controlling the penetration.

The weld width, as measured on the α plane, is affected both by the slag depth and the energy input. Fluctuations in electrode feed rate were observed at electrode feed rates near the lower end of the range studied. These fluctuations caused variations in the energy input and thus caused corresponding changes in weld width.

This effect is shown in Fig. 4 where the appearance of the weld on the α plane is shown both schematically and by actual photomacrographs. In both instances the weld made with the low electrode feed rate is shown at the right. This behavior agrees with the mathematical conclusion that at constant power the penetration depth is most sensitive to welding speed variations at the low end of the travel speed range.[4]

Depth of Pool. Figure 5 is a photomacrograph of the α plane taken at ×6. It shows how the typical segregation substructure in the weld delineates the weld pool profile. Complementary to these observations, a sulfur addition was used in some experiments.

Figure 6 is a sulfur print taken of the α plane and shows how the dark, high sulfur region reveals the shape of the weld pool. A careful comparison between both techniques showed

Table 3—Welding Variables and Experimental Results

Experiment	Electrode feed rate, cm/s (in./s)	Current, A	Voltage, V	Travel speed, ipm	Energy input, kj/in.	Encounter angle, deg	Pool depth H, cm	Pool depth H, (in.)	Weld width bw, cm	Weld width bw, (in.)	Shape factor, θ	HAZ width—locus of: A_{c3}, cm	HAZ width—locus of: A_{c3}, (in.)	Dilution D,%
1	7.0 (2.8)	450	40	0.48	2250	45	1.4	(0.55)	5.4	(2.13)	3.86	1.10	(0.433)	43
2	7.0 (2.8)	450	40	0.48	2250	35	1.3	(0.51)	5.0	(1.97)	3.85	1.18	(0.465)	—
3	7.0 (2.8)	450	40	0.48	2250	58	1.2	(0.47)	5.0	(1.97)	4.17	—		—
4	11.0 (4.3)	600	40	0.75	1920	—	2.6	(1.02)	5.9	(2.38)	2.27	1.40	(0.551)	43
5	13.5 (5.3)	700	40	0.92	1826	80	2.5	(0.98)	5.5	(2.17)	2.20	—		—
6	13.5 (5.3)	700	40	0.92	1826	83	2.6	(1.02)	5.9	(2.32)	2.27	1.25	(0.492)	—
7	19.0 (7.5)	900	40	1.30	1662	110	3.1	(1.22)	5.0	(1.97)	1.61	1.00	(0.394)	41
8	19.0 (7.5)	900	40	1.30	1662	92	3.8	(1.50)	5.4	(2.13)	1.42	0.95	(0.374)	37
9	19.0 (7.5)	900	40	1.30	1662	115	3.9	(1.54)	4.5	(1.77)	1.15	—		—
10	19.0 (7.5)	900	40	1.30	1662	120	3.3	(1.30)	6.0	(2.36)	1.82	—		—
Complementary experiments														
11	11.0 (4.3)	600	35	0.75	1680	60	1.8	(6.71)	4.2	(1.65)	2.33	1.15	(0.453)	—
12	11.0 (4.3)	600	55	0.75	2640	75	3.5	(1.38)	7.5	(2.95)	2.14	1.40	(0.551)	58

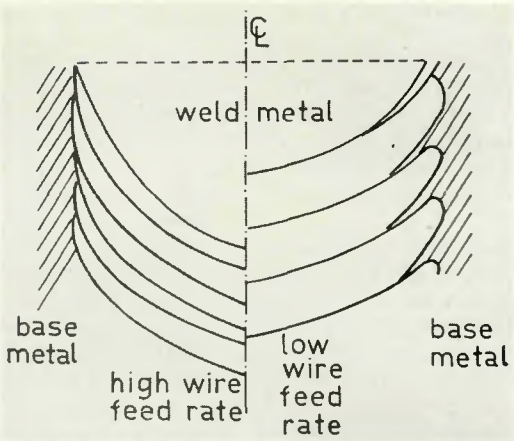

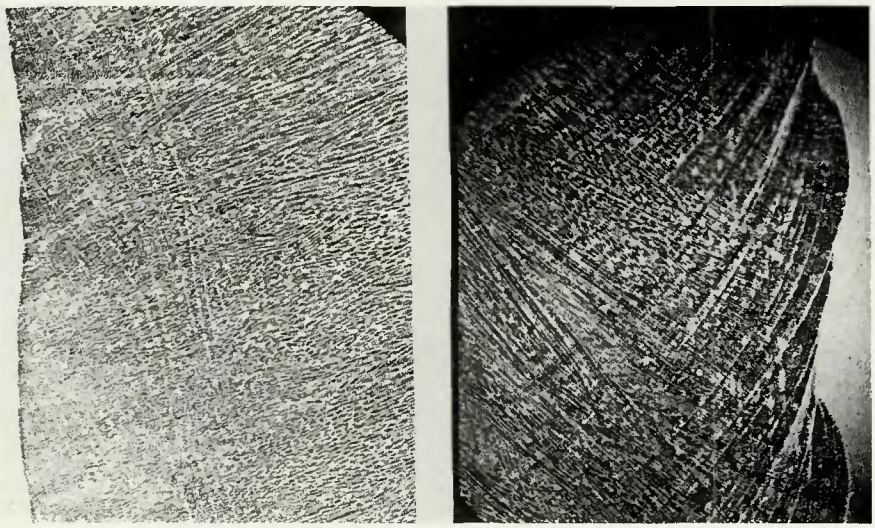

Fig. 4—a (top) Schematical representation of the penetration variation with the welding speed; b (bottom) variation of the penetration with the current intensity: experiment 1 (left) V = 40, I = 450 A; experiment 8 (right) V = 40, I = 900 A

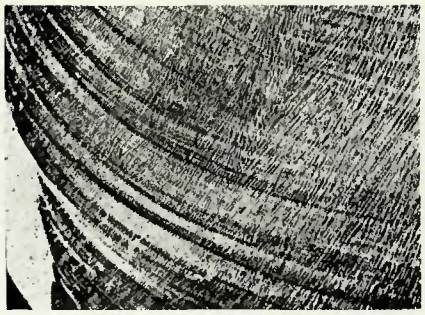

Fig. 5—Metallographic analysis of experiment 6. The etch reveals the segregation substructure and shows the pool shape. ×6 (reduced 50% on reproduction)

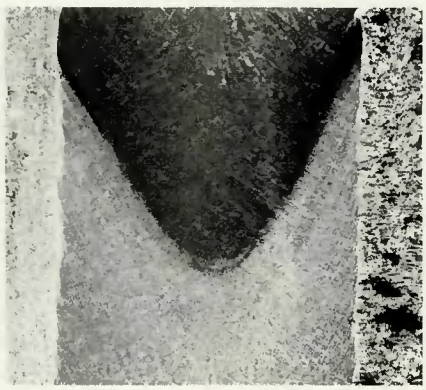

Fig. 6—Shape of the pool revealed in experiment 9 through a sulfur print

excellent agreement. Both techniques were able to reveal an increment in the pool depth H when the electrode feed rate was increased.

Shape Factor. δ is a useful parameter for describing the geometry of the liquid pool. The relative orientation of the grains, and therefore the encounter angle, can be related to the shape factor. Inspection of Table 3 indicates that at a constant voltage of 40 V the shape factor, δ, is inversely related to the electrode feed rate. Note that the shape factor varied from an average of 1.50 with an electrode feed rate of 19 cm/s (7.5 in./s) to about 4 with an electrode feed rate of 7 cm/sec (2.8 in./s).

The complementary experiments show that, when the electrode feed rate is held constant, the shape factor is essentially independent of the welding voltage.

Cross Sectional Area of the Pool. In general the weld pool has the shape of a somewhat distorted paraboloid of revolution. Figure 7 is a schematic showing the type of distortion of the solid liquid interface reported to be common in electroslag melting.[11] A similar distortion occurs near the center of an electroslag weld where a decrease in the rate of heat extraction caused by the increased length of the heat flow path results in a decrease in the growth rate at the solid liquid interface.

Referring again to Fig. 7 and recalling that the travel speed, V, is constant, since the growth rate R is given by $R = V \cos \theta$ a decrease in R must result in an increase in θ. This is shown schematically in Fig. 7 for the growth vectors R_1 and R_2 corresponding to the theoretical and actual growth conditions, respectively.

Figure 8 corresponds to another distortion which appears near the water cooled shoes. This distortion is accentuated by decreasing the pool depth. It is also related to the liquid flow within the weld pool.

Dilution. The calculated values of this parameter ranged from 39 to 58% and increased as the energy input increased.

Effect of Electrode Feed Rate on Welding Speed

For each experiment, the values of travel speed were calculated from electrode feed rate data. For this study, the travel speed ranged from 1.45×10^{-2} and 5.5×10^{-2} cm/s (0.34 and 1.30 ipm)—Table 3.

Effect of Electrode Feed Rate on Energy Input

At constant voltage and weld gap, the energy input is also determined by the electrode feed speed. At 40 V the energy input ranged from 2250 kJ/in. (886 kJ/cm) with 7 cm/sec electrode feed rate to 1662 kJ/in. (654 kJ/cm) with 19 cm/sec wire feed speed.

Effect of Electrode Feed Rate on Macrostructure

The columnar structure in the solidified metal of the weld originated both by epitaxial growth from the partially melted grains of the base metal and also by the nucleation on the refrigerated shoes. The grains grow in the easy growth direction which is most nearly parallel to the direction of heat extraction. Thus growth tends to occur approximately perpendicular to the surface of the pool. Consequently, the shape of the pool controls the angle of the grain growth direction with relation to the axis of the weld, and thus controls the value of the encounter angle.

The importance of the value taken by this angle arises from the fact that a

higher angle produces a greater centerline segregation and, as a consequence, a higher susceptibility of centerline hot cracking.[1] In the present work, encounter angles between 35 and 120 deg were observed. With constant voltage the smaller values correspond to the smaller electrode feed rate range (see Table 3). Figure 9 corresponds to a macrostructure on the β plane (refer to Fig. 2 for orientation) and shows a cross section of a fine columnar structure in a low carbon steel.

Effect of Electrode Feed Rate on Microstructure

Solidification Substructure. By applying special metallographic techniques, the structure and substructure of the weld have been investigated as well as the transition zone between the weld and the HAZ. At the same time, the mechanism of metal transfer from the base metal to the liquid pool can be understood by close examination of the segregation substructure.

Figures 10 and 11, obtained by metallographic etchants developed by Savage et al,[13] clearly show that, similar to other welding processes, the boundary between the two zones is not a line. Instead, it is a transition region composed of a zone melted without mixing and a partially melted zone identified by the segregation substructures clearly shown in Fig. 11. In that region, phases and inclusions of low melting point have been melted during the thermal cycle of the process.

The substructure of the weld metal in the 100% mixed region corresponds to a cellular dendritic type. For a constant energy input, the average cell spacing increased from the water cooled shoes or base metal to the weld centerline—Fig. 8. Decreasing the electrode feed rate causes the average cell spacing to increase throughout the weld due to the disminished cooling rate, as Fig. 12 clearly shows. This result agrees with the conclusion of other authors in the sense that the choice of welding conditions influences the pattern of microsegregation.[19]

Mechanism of Metal Transfer from the Base Metal to the Liquid Pool. The metallographic analysis with the different etchants used gives information about the mechanism of material transfer from the base metal to the molten pool.

In all the experiments carried out, the transition between weld and HAZ is characterized by a structure similar to that shown in Fig. 13a. Light etching projections entering the weld region with contour related to the shape of the pool appear at the base metal interface. These projections always had an etching behavior identical to that of the base metal. However, the same type of solidification substructure appears in both these projections and in the dark etching region of the weld, indicating that the segregated solidification substructures are common to both regions—Fig. 13b.

These results suggest that the projections are an extension of the unmixed melted zone.[20] However, the projections are more prominent when the travel speed is low. Figure 4 shows how the pool depth influences the formation of these projections. Note that at low electrode feed rates, and therefore at low travel speeds, the projections become longer and the weld interface more irregular in shape.

Some experiments in which the welding current was interrupted were helpful in understanding the mechanism of material transfer from the base metal to the weld pool. Figure 14 consists of α plane macrographs of two such welds showing the geometry of the slag-pool at the instant the current was interrupted. In each case the left hand side of the macrograph corresponds to the weld centerline. The weld at the left, which was made with 40 V and a travel speed of 1.22 cm/min (0.48 ipm), exhibited a shape factor of 4.17. That at the right was made with 55 V and a travel speed of 1.91 cm/min (0.75 ipm) and had a shape factor of 2.14.

In the weld with the higher shape factor (made with the lower travel speed), the slag pool encroaches upon the base metal to a greater degree and produces a pendulant overhang on which a layer of molten base metal adheres by surface tension.

Figure 15 shows, in schematic form, the mechanism proposed to explain the formation of the projections of unmixed molten base metal. First, the depth of the stagnant boundary layer (shown by the dashed line above the solid-liquid interface) is controlled by the amount of convective mixing in the liquid and is thus controlled by the depth of the molten pool and the

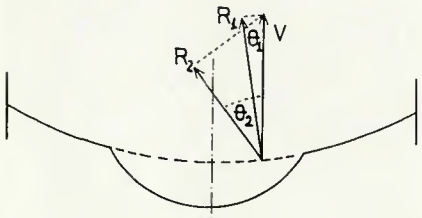

Fig. 7—Distortion of the pool shown schematically. The decrease in the rate of heat extraction at the central zone of the weld produces a decrease in R. As a consequence, θ increases in order to satisfy the expression $R = V \cos \theta$.

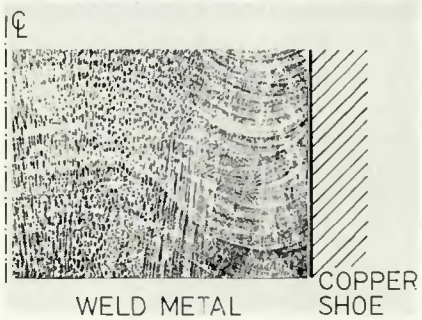

Fig. 8—Distortion near the refrigerated shoes revealed through metallographic etching—experiment 2. ×6 (reduced 75% on reproduction)

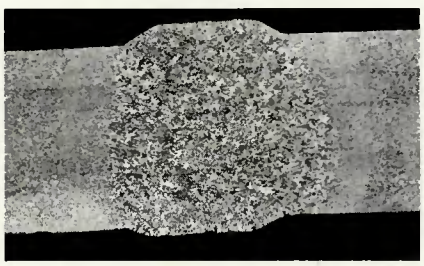

Fig. 9—Macrographic structure observed on plane β. Etching with nital reveals the structure of the weld and HAZ. Original reduction 30% (reduced 46% further on reproduction)

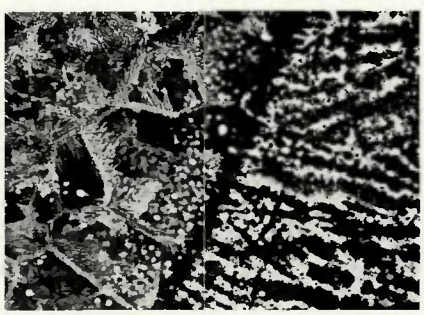

Fig. 10—Boundary between the weld and the HAZ. The segregated solidification substructure of the weld zone is noticeable and the partially melted zone is also revealed by the segregation substructure. ×100 (reduced 50% on reproduction)

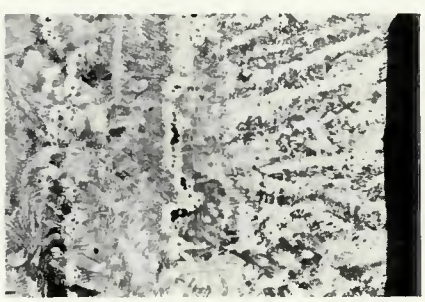

Fig. 11—Detail view of the weld interface showing the fusion zone and the partially melted zone. ×100 (reduced 50% on reproduction)

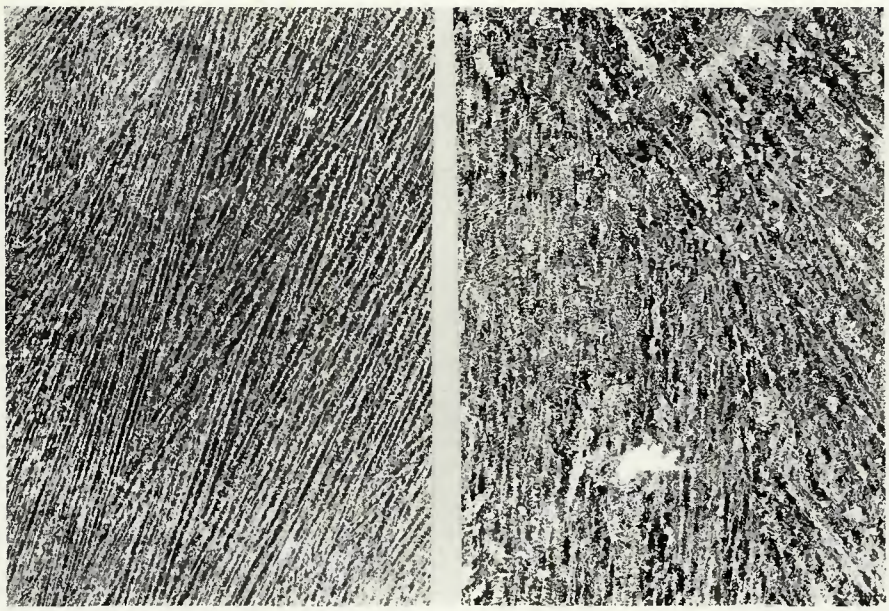

Fig. 12—Comparison between coarse (exp. 12) and fine (exp. 11) substructure of two welds made with different energy inputs. ×6 (reduced 50% on reproduction)

travel speed. In general, decreasing the pool depth, H, increases the thickness of the boundary layers and permits the layer of molten base metal (shown in black in Fig. 15) to slide under the stagnant layer periodically and thus form an unmixed projection of the type shown at right in Fig. 4b.

Increasing the travel speed both increases the depth of the pool H and the rate of solidification R. Increasing H decreases the thickness of the boundary layer owing to more effective convective mixing, and increasing R decreases the time available for the molten layer of base metal to slide into the weld pool. Thus, the projections become shorter and thinner as the travel speed is increased.

Encroachment of the slag pool into the base metal produces a pendulant overhang such as is indicated in Fig. 15 (and at the right in Fig. 14). When this occurs, the molten base metal adhering to the overhang can flow down the overhang, as indicated at A in Fig. 15, to form drops which ultimately are transferred to the liquid metal pool. In summary, for high penetration welds both mechanisms are operative, but for lower values of penetration, only the "projection" mechanism acts.

Welding HAZ Dimensions and Structure. The approximate gradient in the peak temperature experienced in the HAZ was determined from macrographs on the α plane similar to the one shown in Fig. 16. The fusion boundary is visible at the left and represents the locus of the region experiencing temperatures in excess of the liquidus. Near the center of Fig. 16, an abrupt transition occurs from an extremely fine grain size at the left to a coarser grain size at the right. This abrupt change in grain size identifies the locus of the region experiencing a peak temperature approximately equal to the A_{c3} transition temperature. Thus, by measuring the distance from the weld interface to this location, an indication of the effect of welding variables on the extent of the HAZ could be obtained.

From such measurements, the distance to the locus of the A_{c3} was found to vary from 0.95 cm (0.374 in.) for a weld made with an energy input of 1662 kJ/in. to a maximum of 1.4 cm (0.551 in.) for a weld made with an energy input of 2640 kJ/in. Table 3

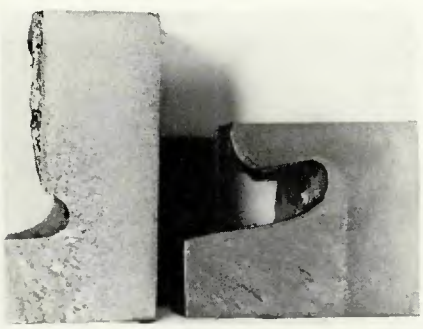

Fig. 14—Comparison of the shape of the welds on plane α for experiments 3 and 12. ×1.8 (reduced 51% on reproduction)

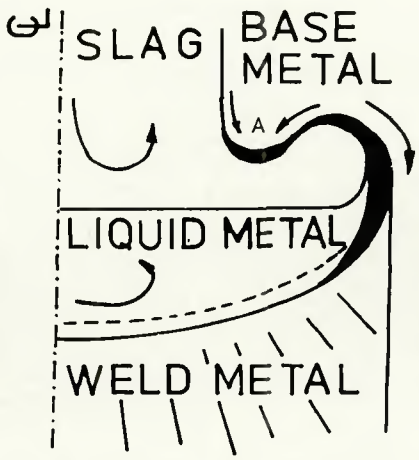

Fig. 15—Schematic representation of both mechanisms of metal transfer

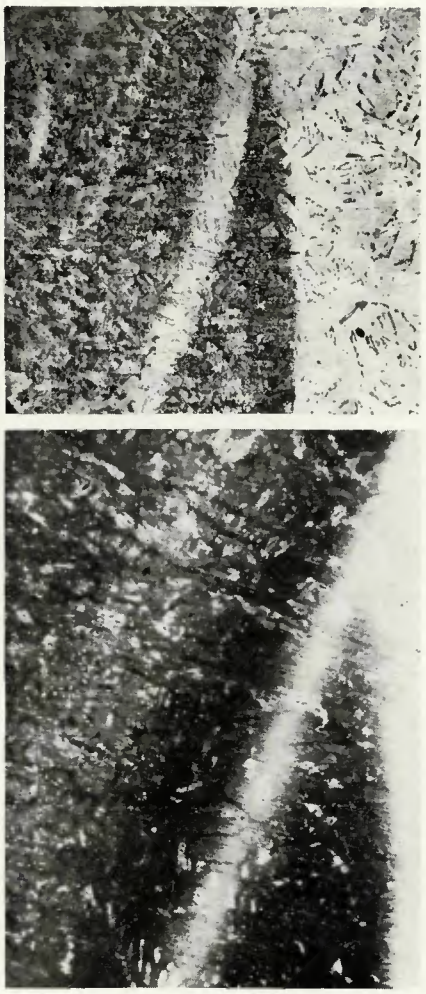

Fig. 13—Metallographic structure observed on plane α: a (top)—shows the projections of the unmixed fusion zone; b (bottom)—shows the presence of a segregated solidification substructure in the projections. ×100 (reduced 46% on reproduction)

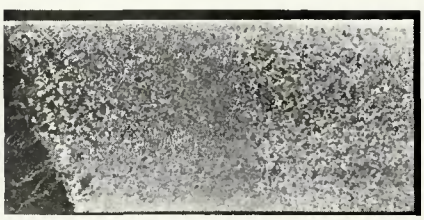

Fig. 16—Metallographic structure of the HAZ. Etching with nital reveals the weld metal, coarse grained region, refined zone, partially refined zone and unaffected base metal. ×6 (reduced 51% on reproduction)

summarizes these data in the next to the last column.

Conclusions

Macroscopic studies of the solidification structure in ESW of low carbon steel showed that when the electrode feed rate was increased at constant voltage:

1. The penetration remained approximately constant.
2. The pool depth increased.
3. The shape factor decreased.
4. The encounter angle increased.
5. The pool shape remained approximately a paraboloid of revolution.

Microscopic studies of the microstructure indicated that:

1. A transition zone at the edge of the weld consists of an unmixed molten zone and a partially melted zone.
2. By increasing the energy input the average dendritic cell diameter was increased.
3. Owing to fluctuations in the speed of the electrode feed, fluctuations in the specific power occur resulting in penetration variations and fluctuations of the solidification rate. These fluctuations can be detected metallographically by suitable etchants.
4. The fluctuations in the solidification rate cause transfer of molten base metal to the liquid pool by sliding through the stagnant boundary layer existing in contact with the S-L interface. This molten base metal does not mix with the rest of the liquid. As a consequence, it can be considered as a projection of the unmixed molten region. Increasing the pool depth and solidification rates decreased the length and thickness of the projections.
5. The mechanism of metal transfer from the base metal to the liquid pool depends upon the penetration of the slag pool into the base metal. In addition, when the penetration becomes large enough to produce a pendulant overhang in the base metal, molten droplets form and are transferred through the slag to the weld pool. At low travel speed both mechanisms are effective.

Acknowledgments

The present work was partially supported by the Multinational Program of Metallurgy sponsored by the Organization of American States (OAS) and the Servicio Naval de Investigación y Desarrollo (SENID) of the Argentine Navy. The authors thank Prof. W.F. Savage for helpful discussions and comments, as well as Eng. L.A. de Vedia and Eng. H. Scagnetti for helpful interactions during different parts of the present work.

References

1. Paton, B., *Electric Slag Welding*. Foring Languages, Publishing House, Moscow.
2. Ellis, D.J., and Gifford, A.F., "Application of Electroslag and Consumable Guide Welding," *Weld. and Met. Fab.*, June 1973, 41 (6), pp. 198-203.
3. Patchett, B.M., Collings, F.W., and Apps, R.L., "Process Parameters and Mechanical Properties of High Speed Consumable Guide Welds," *Weld. and Met. Fab.*, June 1973, 41 (6), pp. 216-224.
4. Eregin, L.P., "Calculating the Penetration in ESW," *Weld Prod.*, July 1970, vol. 17, N°7.
5. Eregin, L.P., "Influence of ESW Setting on the Thermal Cycle in HAZ," *Weld Prod.*, Feb. 1971, Vol. 18, N°2.
6. Prokhorov, N.N., *et al.*, "The Spatial Macrostructure of Weld Metal with Various Forms of Crystallization Front," *Weld Prod.*, 1969, No. 12, pp. 2-7.
7. Granjon, H., et Dadian, M., "Particularitees de la Solidification des Soudures par Fusion," *Soud. Tec. Conn.*, May 1972, Vol. 26 S/6, pp. 181-195.
8. Savage, W.F., Lundin, C.D., and Aronson, R.H., "Weld Metal Solidification Mechanics," *Welding Journal*, 44 (4) April 1965, Res. Suppl., pp. 175-s to 181-s.
9. Lewis, D.M., "Techniques for the Investigation of Thermal Conditions in Continuous Casting," *Journal of the Institute of Metals*, 1953-54, Vol. 82, pp. 395-413.
10. Mitchell, A., "Theory and Practice of Electroslag Remelting," *The Journal of Vacuum Science and Technology*, 1970, vol. 7, N°6.
11. Mitchell, A., *et al.*, "Macrosegregation, Liquid Movement and Heat Flow in ESR Process," *Proceeding of the Fourth International Symposium on ESR processes*. June 1973, Japan.
12. Savage, W.F., Lundin, C.D., and Chase, T.F., "Solidification of Fusion Welds in Face-Centered Cubic Metals," *Welding Journal*, 47 (11) Nov. 1968, Res. Suppl., pp. 522-s to 526-s.
13. Pepe, J.J., and Savage, W.F., "Effects of Constitutional Liquation in 18 Ni Maraging Steel Weldments," *Welding Journal*, 46 (9), Sept. 1967, Res. Suppl., pp. 411-s to 422-s.
14. Biloni, H., Report PMM/R-66 CNEA, Argentina. Report PMM/R-136 CNEA, Argentina.
15. Biloni, H., "The Solidification of Metals," ISI Publication, p. 110, p. 74 (1968).
16. Scagnetti, H.J., de Vedia, L., Solari, M., y Biloni, H., "Soldadura de Grandes Espesores por Electroescoria," Report PMM/C-134. CNEA, Argentina, 1974.
17. Solari, M., y Biloni, H., "Morfología de la Pileta Líquida en Procesos de Refusión y Soldadura por Electroescoria," Report PMM/C-150, CNEA, Argentina 1974.
18. Nippes, E.F., Savage, W.F., and Owczarski, W.A., "The Heat-Affected Zone of Arc-Welded Ductile Iron," *Welding Journal*, 39 (11), Nov. 1960, Res. Suppl., pp. 465-s to 472-s.
19. Hrubec, R.J., "An Investigation of the Effect of Welding Parameters on Segregation and Cracking in HY-80," Thesis, Rensselaer Polytechnic Institute, Troy, N.Y. 1967.
20. Savage, W.F., and Szekeres, S., "Technical Note: A Mechanism for Crack Formation in HY-80 Steel Weldments," *Welding Journal*, 46 (2), Feb. 1967, Res. Suppl., pp. 94-s to 96-s.